Available online at www.sciencedirect.com

SciVerse ScienceDirect

Journal of Magnesium and Alloys 1 (2013) 101−114
www.elsevier.com/journals/journal-of-magnesium-and-alloys/2213-9567

Full length article

Mathematical modeling of thermo-mechanical behavior of strip during twin roll casting of an AZ31 magnesium alloy

Amir Hadadzadeh*, Mary A. Wells

Department of Mechanical and Mechatronics Engineering, University of Waterloo, 200 University Avenue West, Waterloo, ON N2L 3G1, Canada

Received 29 March 2013; accepted 22 April 2013

Abstract

The effect of set-back distance on the thermo-mechanical behavior of the strip during twin roll casting (TRC) of an AZ31 magnesium alloy was modeled using finite element method (FEM). Model validation was done by comparing the predicted and measured exit strip surface temperature as well as the secondary dendrite arm spacing (SDAS) through the thickness of the sheet to those measured during experiments. Model results showed as the set-back distance increases, the strip exit temperature decreases and the solidification front moves toward the entry of the roll gap. The cast strip also experiences more plastic deformation and consequently, the normal stress on the strip surface and effective strain at the strip center-line increase. Moreover, higher separating forces were predicted for longer set-back distances. Model predictions showed that changing the set-back distance by varying the final thickness has a more significant effect on the temperature and stress-strain fields than altering the nozzle opening height.

Keywords: Twin roll casting process; AZ31 magnesium alloy; Thermal-fluid-stress model; Set-back distance; Roll separating force

1. Introduction

Currently, most magnesium application in the automotive industry is limited to die casting due to the low formability of magnesium. The twin roll casting (TRC) process is an alternative near net shape manufacturing process for producing magnesium sheet since it integrates casting and hot rolling into one process. TRC typically produces magnesium sheets with thicknesses of 2−10 mm. Zhao et al. [1] reported that during the TRC process, the sheet will experience solidification cooling rates in the range of 10^2−10^3°C/s. Di et al. [2] observed that this high cooling rate leads to a more uniform distribution of γ-phase in the as-cast microstructure of twin roll cast AZ31 in compare to Direct Chill (DC) casting. Nakaura et al. [3] investigated the secondary dendrite arm spacing (SDAS) achieved during AZ31 TRC which ranged 5−6.5 μm, while the averaged SDAS obtained by DC casting is around 34 μm.

To date some thermal-fluid models have been developed for TRC of magnesium alloys by coupling transport phenomena with solidification effects. Zhao et al. [1] obtained the flow field and temperature distribution in the strip for AZ31 magnesium alloy by developing a thermal-fluid FEM model to analyze the effect of casting speed, strip final thickness, heat transfer coefficient and casting temperature. Bae et al. [4] studied the effect of nozzle configuration and casting speed on the temperature distribution and flow field in the roll bite region by developing a 2-D thermal-fluid finite difference model for vertical twin roll casting of AZ91 magnesium alloy. A CFD model was developed by Zeng et al. [5] to predict the

* Corresponding author. Tel.: +1 519 888 4567x38743.
E-mail addresses: ahadadza@engmail.uwaterloo.ca (A. Hadadzadeh), mawells@uwaterloo.ca (M.A. Wells).
Peer review under responsibility of National Engineering Research Center for Magnesium Alloys of China, Chongqing University

Production and hosting by Elsevier

http://dx.doi.org/10.1016/j.jma.2013.04.001

fluid flow and temperature distribution during twin roll casting of AZ31 with an asymmetric nozzle which provided different contact lengths on the upper and lower rolls.

In the current study, a thermal-fluid-stress model has been developed for AZ31 magnesium alloy TRC process using the finite element method (FEM). This model is capable of coupling transport phenomena to stress-strain development in the cast strip. The aim of the study was to analyze the effect of set-back distance on the thermo-mechanical behavior of the AZ31 strip during TRC. Strip exit temperature, normal and shear stress development on the strip surface, effective strain at the center-line and roll separating force were studied for different casting speeds and set-back distances. Both nozzle opening height (entry thickness) and roll gap (final thickness) were varied to change the set-back distance.

2. Experimental procedure

The TRC facility was studied for this research is currently the only facility in Canada capable of producing twin roll cast magnesium. The facility is based at CanmetMATERIALS located in Hamilton, Ontario, Canada. The roll diameter of the facility is 355 mm. The rolls are made from tool steel H13 and the facility has the ability to achieve speeds up to 6.0 m/min. The thickness of the cast strip can vary between 2 and 8 mm and the width of the strip ranges in 150−250 mm.

The commercial AZ31 magnesium alloy ingots were melted in an electric resistance furnace under protective gas, a mixture of SF_6 and N_2. The molten material was then transferred to the headbox using a melt delivery system. The temperature of the molten material at the headbox was monitored and maintained at the desired value. The gap between the two rolls was set to the desired strip thickness and once the temperature of the nozzle reached an appropriate value (∼700−740°C), the molten magnesium was fed through the nozzle to the roll bite region. Melt temperature in the furnace, melt level and temperature in the headbox, nozzle temperature, strip surface temperature at the exit point of the caster, casting speed, roll surface temperature and coolant water temperature were acquired during the process. In total, eight TRC trials were conducted under varying casting temperature, casting speed and entry/final thickness conditions as shown in Table 1.

After TRC, the as-cast strips were characterized using optical metallography in terms of microstructure through thickness and secondary dendrite arm spacing (SDAS). The samples were chosen from the mid-width position of the strips and studied through their thickness in the casting direction. To measure the SDAS, the primary dendrite branches were identified and the secondary dendrite arms were considered as those developed from the primary arms; as suggested by Grugel [6] and Turhal and Savaskan [7]. The center-to-center distance between the neighboring arms was then measured to determine the SDAS. In total a minimum of three samples and 60−90 secondary dendrites were analyzed for each test condition to ensure statistically the measurements were accurate.

Table 1
TRC conditions conducted at CanmetMATERIALS.

Trial #	Casting temperature (T_{cast}) (°C)	Casting speed (v) (m/min)	Entry thickness (t_0) (mm)	Final thickness (t_f) (mm)
1	740	2.82	12	5
2	712	2.10	12	5
3	700	2.50	8	5
4	677	1.70	12	6
5	670	2.10	8.5	5
6	666	1.97	8.5	5
7	680	2.50	7.8	5
8	680	3.00	8.8	5

Model validation was done by comparing the predicted and measured strip surface temperature and SDAS through the strip thickness. The temperature of the strip surface at 5cm away from the caster exit was measured using a laser pyrometer for all trials. Cooling rates used for SDAS predictions were calculated by evaluating the solidification time at various positions through the thickness of the strip. According to the work done by Allen et al. [8] the relation between cooling rate and secondary dendrite arm spacing for AZ31 magnesium alloy follows Eq. (1). This empirical relation, which is valid for cooling rate ranges 10^{-1} to 10^{6}°C/s, was used in the current study to correlate the predicted cooling rates and SDAS.

$$\lambda = 35.5\mathrm{CR}^{-0.31} \quad (1)$$

where CR is the averaged cooling rate (in °C/s) and λ is the secondary dendrite arm spacing (in μm).

3. Mathematical model

3.1. Model overview

Fig. 1 shows a 2D schematic of a twin roll caster. ℓ_1 is the set-back distance, the distance between the nozzle entry and the caster kissing point (the point where the least distance between two rolls occurs). Region ① represents 100% liquid metal, region ② shows the mushy zone (the mixture of solid and liquid metal) and region ③ represents the fully solid metal.

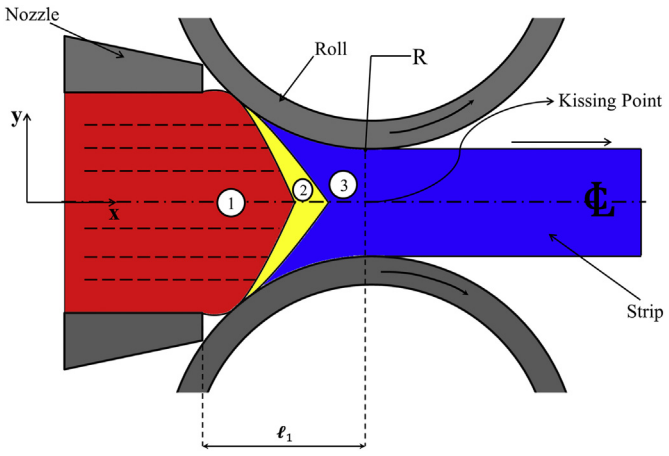

Fig. 1. Schematic of the TRC process, region ① is the liquid metal, region ② is the mushy zone and region ③ is the solid strip, ℓ_1 is the set-back distance. Note: the perspective of the TRC is not to scale and the nozzle size and position are magnified with respect to the rolls.

The following assumptions were made in developing the model:

I. The process is dominated by transport phenomena and deformation in two dimensions. In the third dimension (across the width) there is no significant heat transfer, fluid flow or deformation (plane strain deformation).
II. Due to symmetry only the top half of the strip and part of the top roll was modeled in the simulation.
III. The fluid flow is laminar when exiting the nozzle tip and entering the roll bite.
IV. The rolls are rigid and do not deform elastically.

The important physical phenomena which occur during the process and are integrated in the model include:

I. Heat transfer and fluid flow in the melt sump (liquid metal, zone ① in Fig. 1).
II. Heat transfer, fluid flow and latent heat of fusion release in the mushy zone and deformation in the material once the coherency point is reached, (zone ② in Fig. 1).
III. Heat transfer and plastic deformation in the solid phase (zone ③ in Fig. 1).
IV. Heat transfer from the magnesium sheet to the roll surface, and
V. Heat transfer inside the roll material and from the roll's sleeve to the circulated water.

3.2. Governing equations

In order to model the fluid flow and heat transfer phenomena the basic mass, momentum and energy conservation equations were solved as shown in Eqs. (2)–(4).

- Mass conservation equation:

$$\frac{\partial}{\partial x_j}\left(\rho u_j\right) = 0 \tag{2}$$

- Momentum conservation equation:

$$\frac{\partial}{\partial x_j}\left(\rho u_i u_j\right) = \rho g_i + \frac{\partial}{\partial x_j}\left(\mu \frac{\partial u_i}{\partial x_j}\right) - \frac{\partial p}{\partial x_i} \tag{3}$$

- Energy conservation equation:

$$\frac{\partial}{\partial x_j}\left(\rho u_j C_P T\right) = \frac{\partial}{\partial x_j}\left(k \frac{\partial T}{\partial x_j}\right) \tag{4}$$

where u_i is the ith component of the velocity vector, ρ is density, g is the gravity vector, μ is dynamic viscosity, p is pressure, C_p is material specific heat, k is the thermal conductivity and T is temperature.

Since solidification occurs during the process and the latent heat associated with fusion is released, a modification was applied to the energy conservation equation to account for this effect. Therefore, an equivalent specific heat capacity is defined and implemented to the energy conservation equation, as shown in Eq. (5) [5]. Moreover, the mushy zone (mixture of solid and liquid) acts as a porous medium and affects the fluid flow, this effect is taken in account by adding a source term to the momentum conservation equation and Eq. (3) is modified as shown in Eq. (6) [5].

$$H = H_{\text{ref}} + \int_{T_{\text{ref}}}^{T} C_P \, \mathrm{d}T \tag{5}$$

$$\frac{\partial}{\partial x_j}\left(\rho u_i u_j\right) = \rho g_i + \frac{\partial}{\partial x_j}\left(\mu \frac{\partial u_i}{\partial x_j}\right) - \frac{\partial p}{\partial x_i} - C\frac{(1-f_l)^2}{f_l^3+\varepsilon}\left(u_j - u_{r,j}\right) \tag{6}$$

where H is the enthalpy, H_{ref} reference enthalpy (here the latent heat of fusion), C_P specific heat capacity, T_{ref} reference temperature (here solidus), C is a constant of the liquid phase between 10^4 and 10^7 [9], f_l is the fraction liquid, ε a small number to avoid division by zero when the liquid fraction approaches zero and $u_{r,j}$ is the roll velocity component in the j-direction (in this case it is assumed to be casting velocity in the x-direction and 0 in other directions).

For the thermal elastic-plastic model, the material is defined as an isotropic elastic-viscoplastic material. The velocity field below the coherency temperature which is used to calculate the strain was determined by minimizing the energy functional as shown in Eq. (7) [10].

$$\delta\pi = \int_{\Omega} \delta\boldsymbol{\varepsilon}^* \cdot \sigma \, \mathrm{d}\Omega - \int_{\Omega} \delta\mathbf{u}^* \cdot \rho\mathbf{g} \, \mathrm{d}\Omega - \int_{\Gamma} \delta\mathbf{u}^* \cdot \mathbf{t} \, \mathrm{d}\Gamma = 0 \tag{7}$$

where the superscript "*" denotes the transpose of a vector or matrix, $\mathbf{g}$ is the gravity vector, $\mathbf{t}$ is the force per unit length acting on the boundary Γ, $\delta\mathbf{u}$ and $\delta\boldsymbol{\varepsilon}$ virtual variations of displacement $\mathbf{u}$ and associated strain vector $\boldsymbol{\varepsilon}$, respectively and Ω is the solution domain.

The total strain experienced by the material is subdivided into thermal, elastic and viscoplastic components, as shown in Eq. (8) [11].

$$\boldsymbol{\varepsilon} = \boldsymbol{\varepsilon}_{\text{T}} + \boldsymbol{\varepsilon}_{\text{e}} + \boldsymbol{\varepsilon}_{\text{p}} \tag{8}$$

where $\boldsymbol{\varepsilon}$ is the strain and subscripts T, e and p represent thermal, elastic and viscoplastic components, respectively. Thermal strain is calculated using Eq. (9).

$$\boldsymbol{\varepsilon}_{\text{T}} = -\int_{T}^{T_{\text{Coh}}} \beta(T)\mathrm{d}T \cdot \mathbf{I} \tag{9}$$

where β is thermal expansion coefficient as a function of temperature, $\mathbf{I}$ is the identity tensor and T_{Coh} is the coherency temperature, at which the mushy material has formed and interconnected structure can start to sustain some stress.

Elastic strain below the coherency temperature is calculated using Hooke's law as shown by Eq. (10).

$$\boldsymbol{\sigma}_{\text{e}} = \mathbf{D}(T) \cdot \boldsymbol{\varepsilon}_{\text{e}} \tag{10}$$

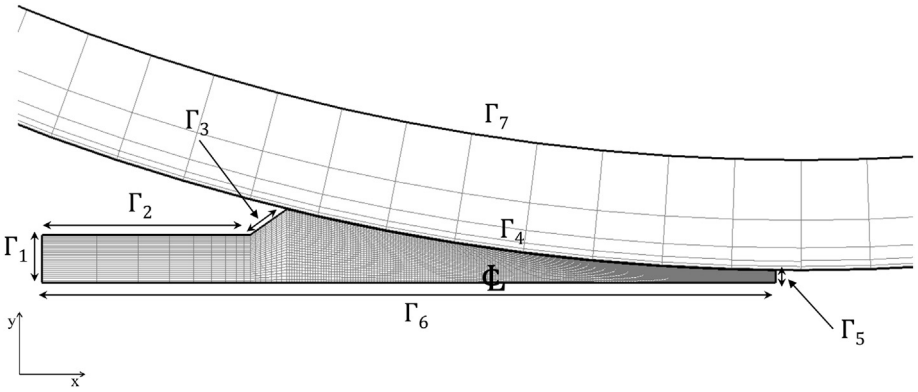

Fig. 2. Boundary regions of the solution domain.

where the material's temperature dependent elastic modulus and Poisson's ratio form the matrix **D** [10,11].

The constitutive behavior of the AZ31 magnesium alloy is modeled using the extended Ludwig equation developed based on some high temperature measurements of AZ31 at a range of elevated temperatures and strain rates [12] as shown in Eq. (11).

$$\boldsymbol{\sigma} = K\left(T\right)\cdot\left(\dot{\boldsymbol{\varepsilon}}_{\mathrm{p}} + \dot{\varepsilon}_{\mathrm{po}}\right)^{m(T)}\left(\boldsymbol{\varepsilon}_{\mathrm{p}} + \varepsilon_{\mathrm{po}}\right)^{n(T)} \tag{11}$$

where $\boldsymbol{\sigma}$ is the stress tensor, $\dot{\boldsymbol{\varepsilon}}_{\mathrm{p}}$ is the strain rate, $\boldsymbol{\varepsilon}_{\mathrm{p}}$ is the strain, K is the strength coefficient, n is the strain hardening exponent and m is the strain rate sensitivity exponent. $\dot{\varepsilon}_{\mathrm{po}}$ and $\varepsilon_{\mathrm{po}}$ are small numerical constants needed to ensure that at a plastic strain of zero, the yield stress of the material is correct.

3.3. Boundary conditions

Fig. 2 shows the boundaries of the solution domain. The following speed and thermal boundary conditions are applied to the domain:

- Inlet (Γ_1): the boundary condition in this region consists of the casting temperature and velocity; Eqs. (12) and (13).

$$V_x = V_{\mathrm{in}},\ V_y = 0 \tag{12}$$

$$T = T_{\mathrm{cast}} \tag{13}$$

where V_x and V_y are the components of velocity in x and y directions, respectively; V_{in} is the inlet velocity and T_{cast} is the casting temperature. The liquid velocity at the inlet is calculated from the casting speed while the mass is conserved during the process.

- Nozzle surface (Γ_2 and Γ_3): this region is assumed to be adiabatic (no heat loss) and that there is a no-slip wall condition (no relative velocity between the fluid and the boundary).

$$V_x = V_y = 0 \tag{14}$$

$$\partial T/\partial y = 0 \tag{15}$$

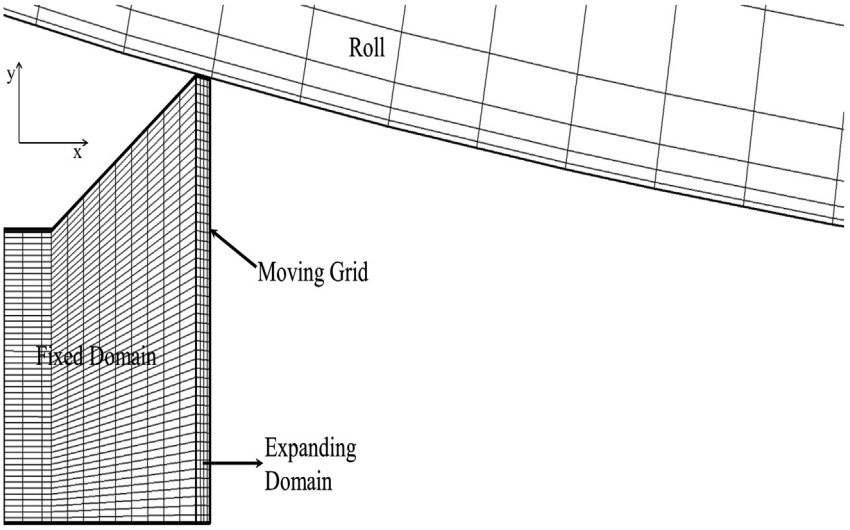

Fig. 3. Solution domain and finite element mesh at $t = 0$ s.

Table 2
Thermo-physical properties of AZ31 magnesium alloy.

Property	Value/function							
Density, ρ (kg/m^3) [16]	1780							
Latent heat of fusion, L (J/kg) [16]	340,000							
Specific heat, C_p (J/kg °C) [17]	$820 + (0.79 \times T) - ((3.6 \times 10^6)/(T - 255)^2)$[a]							
Thermal conductivity, k (W/m °C) [15]	50 °C	100 °C	200 °C	250 °C	424 °C	630 °C	635 °C	680 °C
	83.9	87.3	97.0	101.8	118.5	60	120	240
Solidus, T_{sol} (°C) [15]	424							
Liquidus, T_{liq} (°C) [15]	635							
Coherency temperature, T_{Coh} (°C) [18]	578[b]							

[a] Temperature in Kelvin.
[b] At a fraction solid of 0.9.

- Roll/strip interface (Γ_4): in this region a no-slip rotating wall is defined. The heat transfer between the roll and the strip is defined using a heat transfer coefficient (HTC) as shown in Eq. (16). For the analysis it was assumed that HTC's value remained constant from the first point of contact of the liquid against the roll surface to the exit of the strip from the rolls.

$$-k\frac{\partial T}{\partial n} = \mathrm{HTC}(T_s - T_0) \tag{16}$$

where k is the thermal conductivity, T is temperature, HTC is the heat transfer coefficient, n is the normal direction to the strip surface, T_s is the strip surface temperature and T_0 is the roll surface temperature.

- Outlet (Γ_5): the exit velocity is equal to the casting speed.

$$V_x = V_{cast},\ V_y = 0 \tag{17}$$

where V_{cast} is the casting speed.

- Center-line (CL, Γ_6): the center-line is considered to be a symmetry boundary with no fluid flow or heat transfer across the interface.

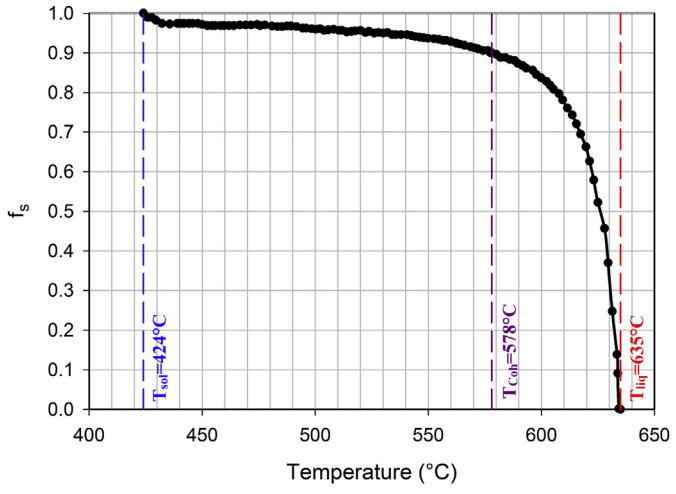

Fig. 4. Non-equilibrium fraction solid (Scheil cooling conditions) for AZ31 magnesium alloy, graph reproduced from Ref. [15].

$$V_y = 0, \partial V_x/\partial y = 0 \tag{18}$$

$$\partial T/\partial y = 0 \tag{19}$$

- Inner roll surface/circulated water interface (Γ_7): there is heat transfer from the roll material to the coolant water inside the roll. Similar conditions of Eq. (16) is governing here, the water temperature is 40°C and the HTC=40 kW/m$^{2\circ}$C is applied.

Besides thermal and fluid boundary conditions, the appropriate mechanical boundary conditions have been assigned to the model. At the free surfaces, i.e., inlet and nozzle surface (Γ_1, Γ_2 and Γ_3), there are no constraints on the displacements. The effect of material constraint at the outlet is simulated by assigning a fixed normal pressure, while at the center-line a fixed normal distributed stiffness plays the same role [13]. The interaction between the cast material and the roll surface at the strip/roll interface, Γ_4, is described using a friction law shown by Eq. (20).

$$\tau_{crit} = \mu P \tag{20}$$

where τ_{crit} is the critical shear stress, P is normal pressure and μ is the coefficient of friction. For the present study a coefficient of friction $\mu = 0.4$ was chosen which is typical for hot rolling.

Table 3
AZ31 magnesium alloy Young's modulus [18].

Temperature (°C)	Young's modulus, E (GPa)	Thermal expansion coefficient, β (10^{-6}/C)
27	45	30.7
102	43	31.4
202	41	32.4
297	38	33.2
342	37	33.7
397	35.5	34.2
424	34.5	34.4
578	15	35.9
608	1	0
632	0	0

Table 4
Parameters represented in Eq. (11) for AZ31 magnesium alloy [12].

Parameter	Temperature (°C)	Value
K	$T < 118$	$-0.0835T + 394.4$
	$394 > T \geq 118$	$-1.1639T + 521.76$
	$T \geq 394$	$-0.5761T + 316.62$
n	$T < 150$	0.38
	$T \geq 150$	$-0.0013T + 0.5769$
m	$T < 168$	$2.89 \times 10^{-5}T - 1.83 \times 10^{-3}$
	$T \geq 168$	$0.00042T - 0.0638$
$\dot{\varepsilon}_{po}$	–	0.0001
ε_{po}	–	0.002382

Table 6
Measured temperatures of the strip surface at the exit point of the caster.

Trial #	Measured strip exit temperature (°C)
1	471
2	397
3	376
4	400
5	290
6	273
7	307
8	350

3.4. Solution domain

For the finite element discretization, rectangular isoparametric elements with four nodes were chosen as depicted in Fig. 3. Since the TRC process is a continuous casting process and a part of the domain is moving with the casting speed, an appropriate coordinate system should be considered. So, the solution domain for the cast material is divided to two subdomains; a fixed domain and an expanding domain. For the fixed domain, which consists of the region inside the nozzle, an Eulerian coordinate system is defined. The expanding domain represents the part of the domain moving inside the roll bite region as the process proceeds. So, an Arbitrary Eulerian Lagrangian (ALE) coordinate system is applied to define the expanding domain and moving grid properly. Moreover, the roll is described by a Lagrangian coordinate system as well. Once the discretized domain is defined it is imported to the commercial FEM package ALSIM [14] in addition to the boundary conditions and material properties to couple and solve the equations to perform modeling.

3.5. Material properties

Thermo-physical properties of AZ31 magnesium alloy, used for the model in the current study, were available in the literature as shown in Table 2. In order to conduct a representative model of the TRC process, the non-equilibrium (Scheil cooling conditions) solidus and liquidus temperatures were used for the AZ31. Values reported by Hao et al. [15], generated by the computational thermodynamics database JMatPro, were used. The Scheil cooling conditions' fraction solid used for latent heat release calculation is shown in Fig. 4. Table 3 illustrates AZ31 Young's modulus and thermal expansion coefficient. Table 4 shows the parameter used in the constitutive equation of AZ31 (Eq. (11)).

3.6. Casting conditions

Table 5 shows the casting conditions modeled in the present study. The purpose of the model is to analyze the effect of casting speed and set-back distance (ℓ_1 in Fig. 1). Set-back distance (SB), is defined as the distance between the nozzle entry and the kissing point and is calculated using Eq. (21).

$$\mathrm{SB} = \ell_1 = \sqrt{(R\Delta t - 0.25\Delta t^2)} \tag{21}$$

where R is the roll radius and Δt is the reduction (the difference between entry and final thickness). As seen in Eq. (21), for a given roll radius (177.5 mm for the current study), varying the reduction changes the set-back distance. To change the reduction the entry thickness could be kept constant and the final thickness varies or vice versa. Both approaches have been used in the present work to analyze three set-back distances of 32.5, 37.5 and 41.8 mm. First the entry thickness was set to 12 mm and the final thickness varied between 2, 4 and 6 mm. In another set of simulations, the final thickness was kept constant at 6 mm and the entry thickness varied to 14 and 16 mm. So for a given set-back distance the effect of both entry thickness and final thickness was quantified.

Table 5
Casting conditions modeled in the present study.

Casting temperature (T_{cast}) (°C)	Entry thickness (t_0) (mm)	Final thickness (t_f) (mm)	Set-back distance (ℓ_1) (mm)	Strip width (mm)	Casting speed (v) (m/min)
677	12	2	41.8	250	1.0–14.0
		4	37.5		
		6	32.5		
	14		37.5		
	16		41.8		

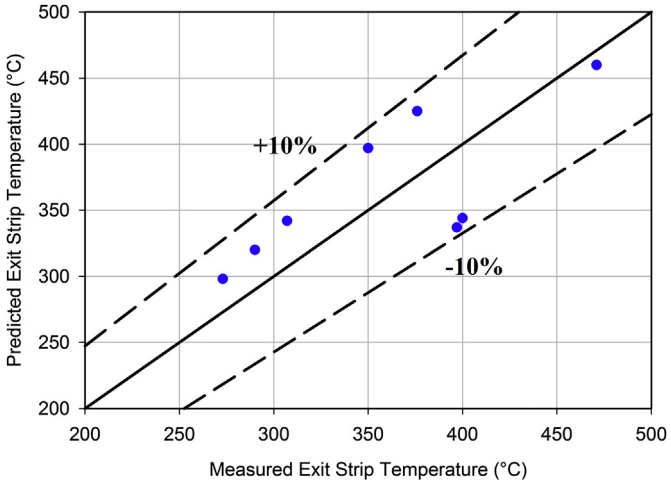

Fig. 5. Comparison of predicted and measured temperature for the conditions shown in Table 1, using HTC = 11 kW/m^2 °C. The solid line shows the perfect match and two dashed lines show ±10% variance from the perfect match.

4. Results and model validation

4.1. Strip surface exit temperature

Table 6 shows the measured strip surface temperature obtained during the experiments. The exit strip temperature represents the overall view of the amount of energy extracted in the roll bite. So, as a part of model validation the model was run using various values for HTC range 10–20 kW/m^2 °C and then the predicted exit temperatures were compared with the measured ones to evaluate the optimum HTC. As shown in Fig. 5, the comparison suggested the optimum value for HTC is 11 kW/m^2 °C since the predicted values match the measured ones in a range of ±10% error.

4.2. As-cast microstructure

Fig. 6 illustrates the typical as-cast microstructure of the twin roll cast AZ31 through the thickness of the strip. The microstructure consists a chill zone at the surface followed by a columnar dendritic zone and an equiaxed zone at the strip center. Fig. 7 illustrates more details of the dendritic microstructure development during TRC of AZ31 magnesium alloy and part of the procedure of SDAS measurement on the optical microstructure. Fig. 8 represents the measured SDAS through thickness versus the predicted values for two trials, using the optimum HTC = 11 kW/m^2 °C. As observed, the largest SDAS occurs at the center-line due to lowest cooling rate and finest SDAS is observed at the strip surface. There is a fairly good agreement (within 20%) between the measured and predicted values. The validation procedure shows the fair accuracy of the model for further assessments.

5. Discussion

5.1. Microstructure evolution

As observed in Fig. 5, at the strip surface, where direct contact between the molten material and roll surface occurs, the cast material experiences the highest cooling rate during the process. Initially, a thin layer of a rapid cooled microstructure is formed on the surface of the strip which is known as the chill zone. Below the chill zone, a columnar dendritic zone develops in the direction of heat removal. Due to the rotation of the rolls these columnar grains incline from the surface to the center of the strip. By growing the columnar zone toward the center of the strip, the solute is rejected to the remaining liquid metal. Due the presence of the solute rich liquid material an equiaxed zone is formed at the strip center.

5.2. Thermal history of the cast strip

Once the molten material enters the space between the rolls and touches the roll surface, heat is extracted from the molten metal and solidification at the surface of the strip starts almost immediately as the material is pulled into the roll bite. The temperature continues to drop as the strip moves through the

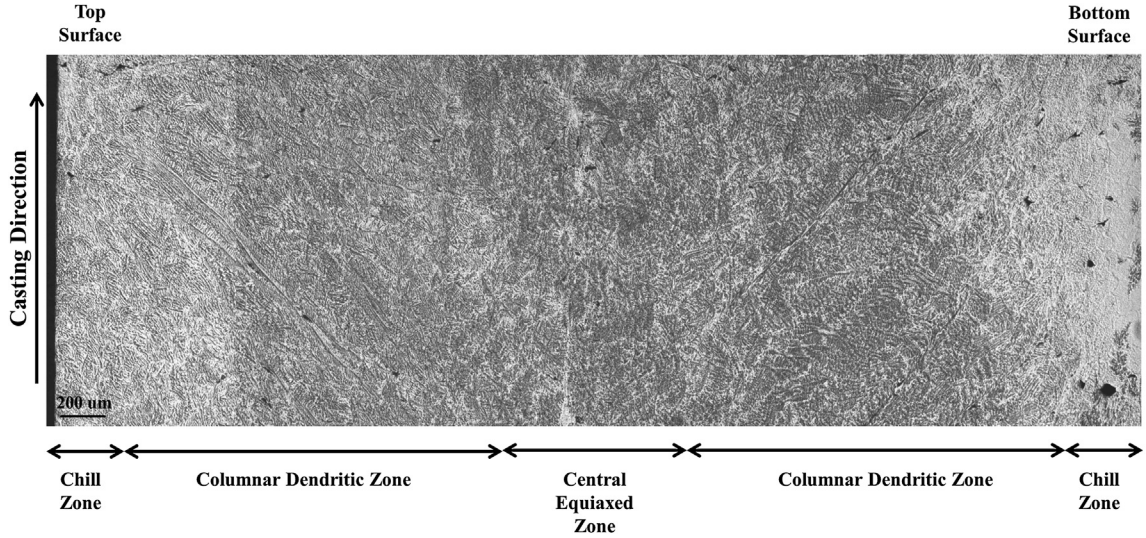

Fig. 6. As-cast microstructure of twin roll cast AZ31 through thickness for trial #3.

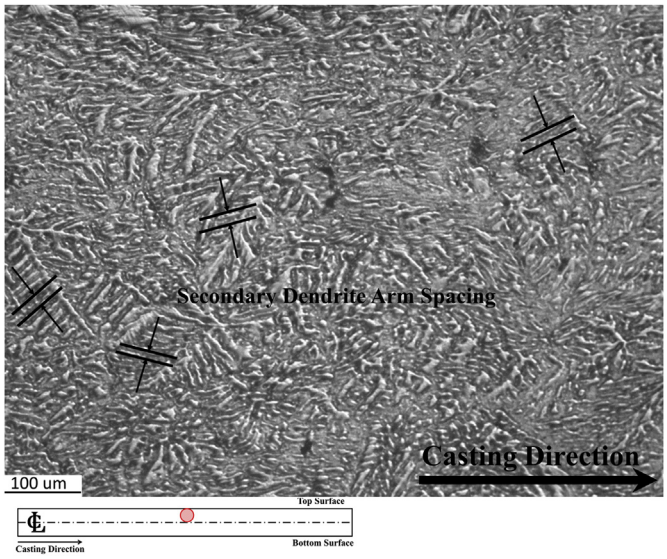

Fig. 7. The procedure of SDAS measurement on the optical microstructure of twin roll cast AZ31, the circle on lower legend shows where the sample has been chosen.

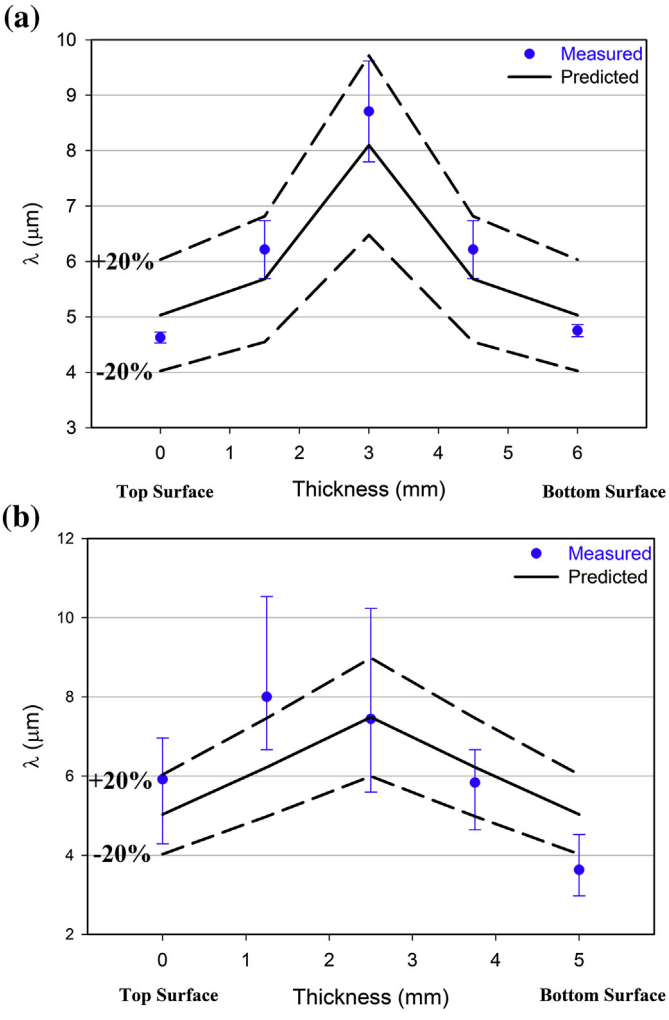

Fig. 8. Predicted (solid line) and measured (symbol) SDAS (λ) through the strip thickness for (a) trial #3 and (b) trial #4. The dashed lines show ±20% variance from the model predictions.

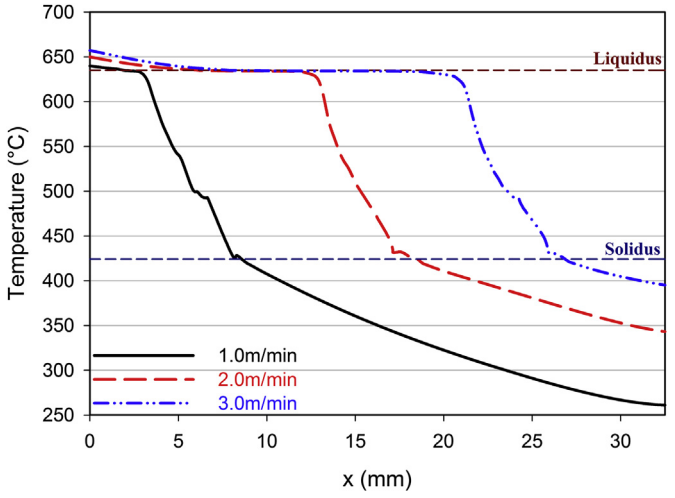

Fig. 9. Model-predicted effect of casting speed on the temperature profile at the strip center-line for $\ell_1 = 32.5$ mm.

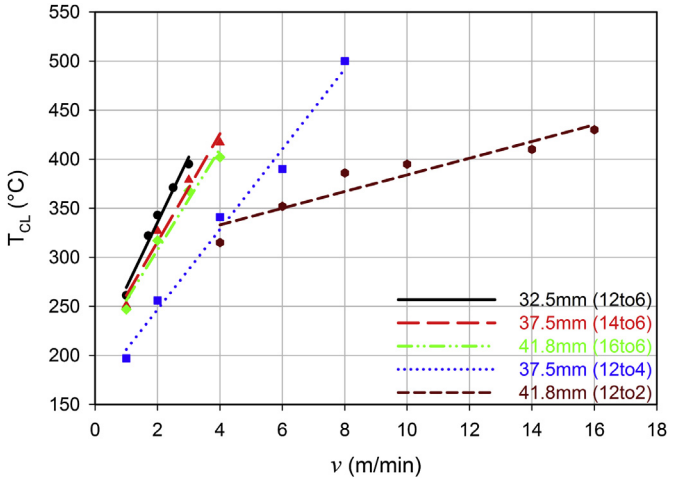

Fig. 10. Model-predicted effect of casting speed (v) and set-back distance on the exit temperature of the strip at the center-line (T_{CL}), the symbols show the predicted values and the lines represent the linear correlation.

roll bite until the solidus temperature is reached and then the solid strip continues to cool and experience plastic deformation.

By increasing the casting speed, less time is provided for heat transfer to occur between the strip and the roll and consequently higher exit strip temperature are obtained. Fig. 9 shows the model-predicted effect of casting speed (v) on the temperature profile at the center-line position for ℓ_1 =

Table 7
The T_{CL}–v relationship.

Set-up no.	t_0 (mm)	t_f (mm)	ℓ_1 (mm)	T_{CL}–v relationship
1	12	6	32.5	$T_{CL} = 66.651v + 202.62$
2	14	6	37.5	$T_{CL} = 55v + 206$
3	16	6	41.8	$T_{CL} = 51.6v + 204.5$
4	12	4	37.5	$T_{CL} = 40.86v + 165.19$
5	12	2	41.8	$T_{CL} = 14.861v + 237.46$

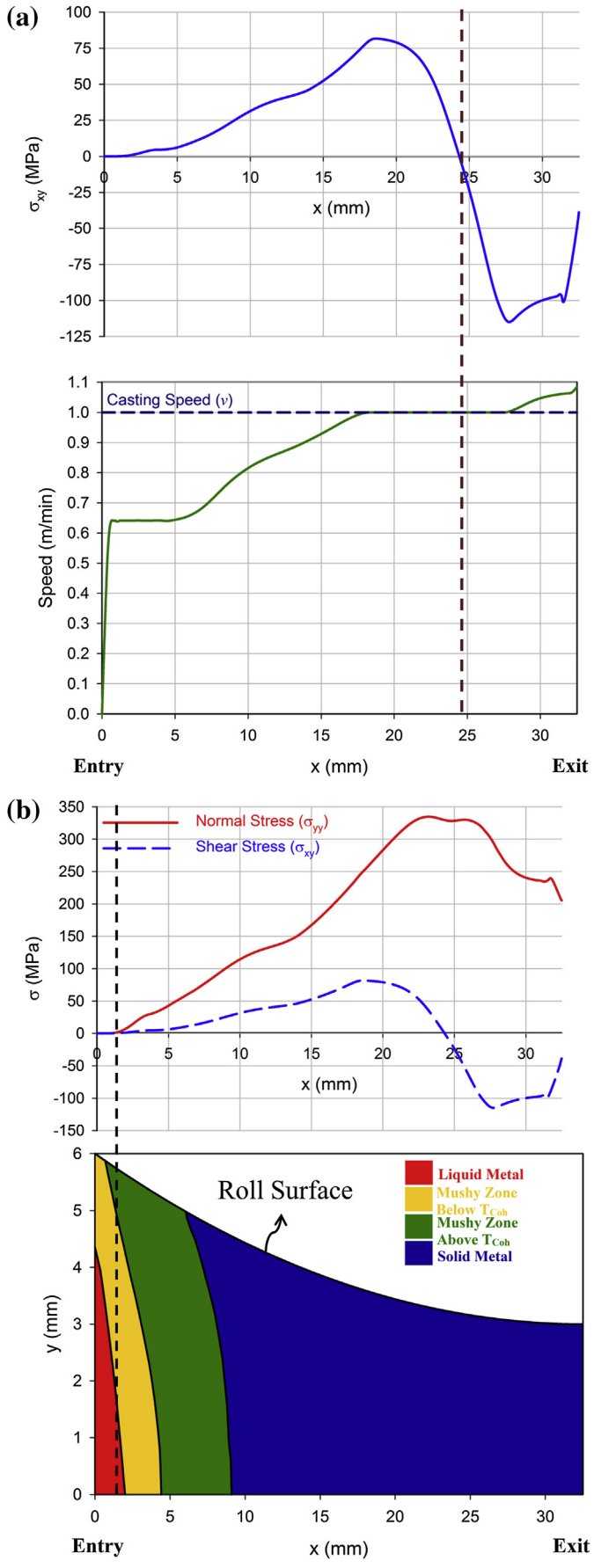

32.5 mm. A plateau can be seen in the temperature history at the liquidus temperature due to the release of the latent heat of fusion as solidification proceeds. Since the casting temperature for all cases is the same, 677 °C, the temperature at the entry for the four cases is almost the same, but at the exit (kissing point) a significant variation in temperature is observed due to the different contact times between the strip and the roll. Moreover, by increasing the casting speed, the solidification front at the center-line is moved further into the roll gap toward the caster exit and the depth of the mushy zone increases as the casting speed increases. The occurrence of the solidification over a longer distance and variations in the strip temperature profile will also affect the stress field development in the solid strip.

Fig. 10 illustrates the model-predicted effect of casting speed (v) on the exit temperature at the center-line (T_{CL}) for various set-back distances. Conducting the process with a longer set-back distance for a given casting speed leads to a lower exit temperature. This is due to providing a longer arc of contact at the strip/roll interface and consequently more heat transfer from the cast metal to the roll material. As the set-back distance increases, the exit temperature becomes more sensitive to the casting speed. Increasing the set-back distance by reducing the final thickness is more effective on the T_{CL} than increasing the entry thickness. As seen in Fig. 10, the slope of T_{CL}–v graph slightly decreases by increasing the entry thickness for a final thickness of 6 mm. Meanwhile, decreasing the final thickness for entry thickness of 12 mm significantly shifts the T_{CL}–v graph toward the horizontal axis. Table 7 illustrates the linear correlation between T_{CL} and v.

5.3. Surface stress development

Similar to a cold or hot rolling process, normal stress (σ_{yy}) occurs on the solidified strip surface during TRC. The normal stress gradually approaches a peak value as the strip approaches the neutral point and then decreases as the strip moves toward the exit region. Beside the normal stress, a shear stress (σ_{xy}) is also developed on the strip surface due to the relative motion between the strip and work rolls, as observed in Fig. 11. The cast material experiences a velocity profile which increases from the entry to the exit point; it moves slower than the rotating rolls prior to the neutral point, reaches the rolls' speed at the neutral point and then travels faster than the rolls beyond the neutral point. The speed profile at the strip surface shows a sudden increase from 0.0 to around 0.63 m/min at the entry region since the material is pulled from the nozzle inside into the roll bite. Since the no-slip conditions govern the nozzle surface, the liquid surface speed at the entry of the roll bite is 0.0 m/min. Continuing along the arc of contact the cast material speed approaches the casting speed (1.0 m/min in this case) and remain at this speed over a

Fig. 11. Model-predicted (a) shear stress (σ_{xy}) development and (b) strip surface stress development (upper graph) and the corresponding liquid–solid profile (lower graph) for $\ell_1 = 32.5$ mm and $v = 1.0$ m/min.

distance due to existence of sticking conditions at strip/roll interface. Near the exit point of the caster the solid material is squeezed out of the caster and experiences an increase in speed. This relative motion at the strip/roll interface leads to positive, zero and negative shear stress prior, at and beyond the neutral point, respectively, as shown in Fig. 11a. Fig. 11b shows the normal and shear stress development on the strip surface for $\ell_1 = 32.5$ mm at $v = 1.0$ m/min as well as the strip solidification contour map in the roll bite. The liquid-solid profile in Fig. 11b illustrates the liquid metal ($f_s = 0$), the non-coherent metal (mushy zone prior to the coherency point; $f_s < 0.9$), coherent metal (mushy zone beyond the coherency point; $f_s \geq 0.9$) and the fully solid metal ($f_s = 1$). The stress does not start to develop immediately at the point where the first fully coherent shell forms on the roll surface. The reason is that the pressure applied to the surface of the strip is transmitted to regions below the solid shell, i.e. in the mushy zone and melt sump. Since the liquid and the non-coherent metal cannot sustain the stress, they do not support the coherent shell and hence no stress is experienced on the surface. Continuing the process, the coherent shell grows and thickens; once an adequate thick shell is reached and enough support is provided for the solid shell, the stress experienced at the surface rapidly increases. Analyzing the stress development for various casting speeds shows that by increasing the casting speed, the thickness of the coherent shell on the roll surface decreases and the stress development at the surface is delayed in the roll gap.

Further analysis of stress development shows that the normal stress indicates a double peak or fluctuation over the peak region. This phenomenon could be due to the interaction between the normal and shear stress. Over the distance where the positive shear stress develops, the normal stress approaches the peak value and once the shear stress approaches to values near zero the normal stress experiences a drop to the lower peak. The lower peak exactly occurs at the position where shear stress is zero. Beyond the neutral point, by decreasing the shear stress to the negative values, the normal stress approaches the second peak and then decreases.

The effect of casting speed on the strip surface normal and shear stress for $\ell_1 = 32.5$ mm is shown in Fig. 12. Casting at higher speeds has two effects; spatial retardation of the stress development toward the exit region and a drop of the peak stress since solidification starts further into the roll bite. Moreover, as the casting speed increases, since less solidified material has undergone plastic deformation and this

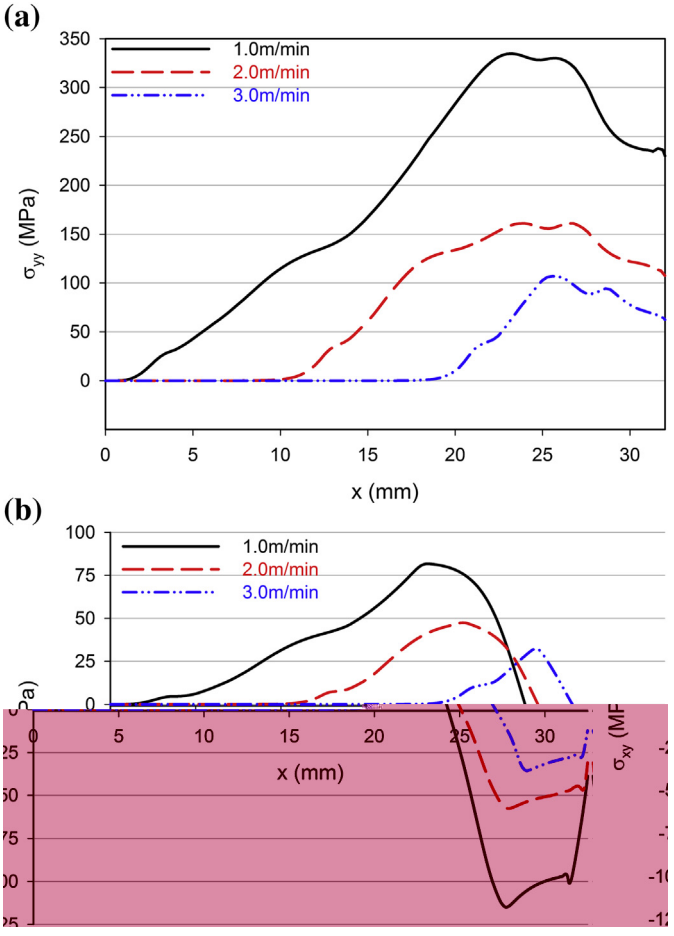

Fig. 12. Model-predicted effect of casting speed on the (a) surface normal stress and (b) surface shear stress for $\ell_1 = 32.5$ mm.

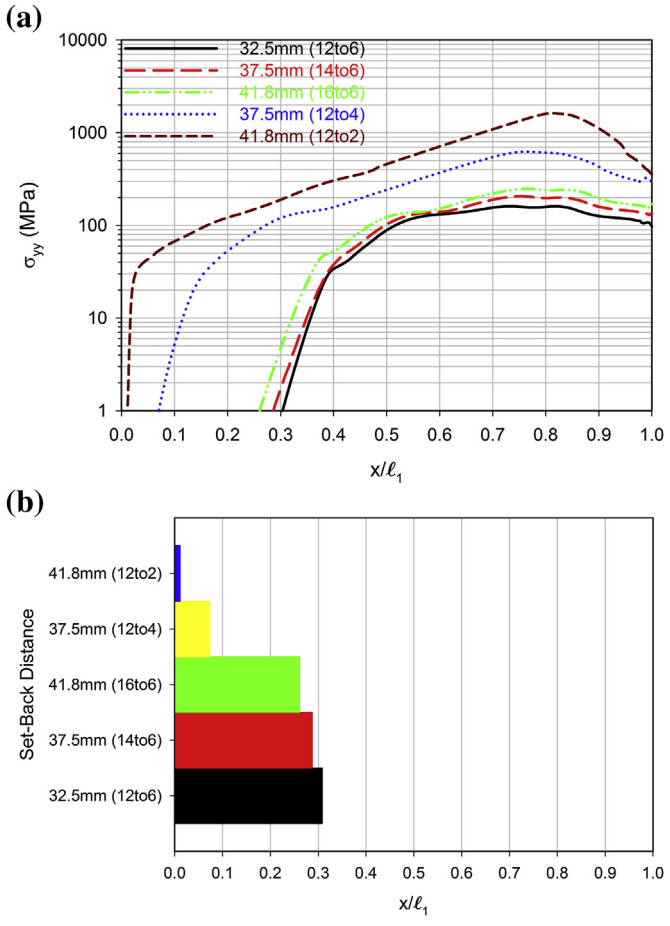

Fig. 13. Model-predicted effect of set-back distance on (a) the surface normal stress and (b) position at which stress begins to develop at $v = 2.0$ m/min.

deformation occurs at higher temperatures, the stress level decreases. Besides, the neutral point shifts toward the exit region by conducting higher casting speeds.

Fig. 13a shows the predicted normal stress on the surface for a range of set-back distances at $v = 2.0$ m/min. The x-position is normalized to account for the entry (0) and exit (1) positions of the strip in the roll bite. The stress profiles shows that reducing the set-back distance leads to lower levels of stress and also a shift in the position in the roll bite where the stress starts to develop, as illustrated in Fig. 13b. The associated solid strip profile and solidification front in the roll bite region for three cases with final thickness of 6 mm is shown in Fig. 14. Increasing the set-back distance decreases the sump depth and moves the solidification front position closer to the roll bite entry. As a consequence the stress experienced by the material starts to develop at a point closer to the entry and goes up to higher peak values since the thickness of the solid material which experience the plastic deformation increases. In other words, the amount of "reduction" during the "hot rolling" part of the TRC process increases by increasing the set-back.

5.4. Roll separating force (SF)

Roll separating force (SF) is the force applied on the work rolls due to the resistance of the material against the deformation and tends to separate the rolls. Fig. 15 shows the modeling results of casting speed's effect on the rolling force per unit width of the strip for different set-back distances. Increasing the casting speed causes lower roll separating force since the amount of solid material which is imposed to the plastic deformation decreases. Moreover, casting with longer set-back distance leads to higher separating force; controlling the set-back distance by the final thickness causes higher separating forces than controlling the set-back distance by the entry thickness.

The relationship between the roll separating force and the casting speed follows an exponential trend in the form of Eq. (22).

$$SF = \alpha \exp(-\beta v) \tag{22}$$

where SF is the separating force per unit width of the strip, α and β constants and v casting speed. Table 8 shows the constants for each set-back distance.

5.5. Effective strain (ε_{eff}) at the center-line

Fig. 16 shows the effective strain at the center-line for $\ell_1 = 32.5$ mm at $v = 1.0$ m/min in conjunction with the strip's liquid–solid profile. The strain development begins immediately at the point where the mushy material meets the coherency temperature. A sharp jump to a plateau is observed

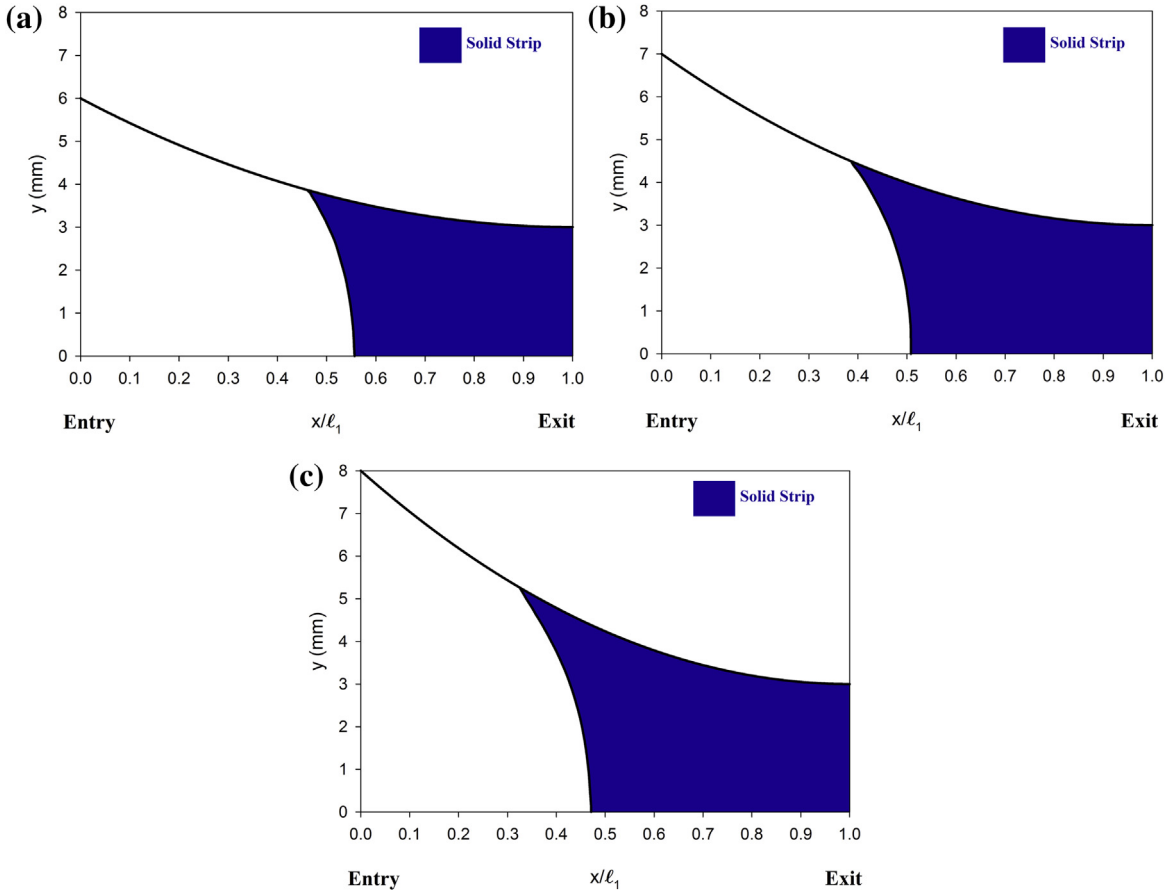

Fig. 14. Model-predicted sump profile for a set-back distance of (a) 32.5 mm, (b) 37.5 mm and (c) 41.8 mm for final thickness of 6 mm.

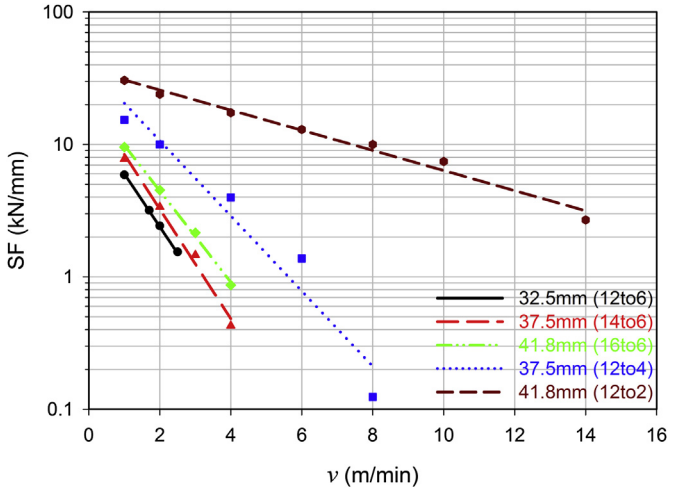

Fig. 15. Model-predicted effect of casting speed (v) on the roll separating force (SF) per strip unit width for different set-back distances, the symbols show the predicted values and the lines represent the exponential correlation.

prior the full solidification; this is due to a high strain rate experienced by the material in this region. The assessment of the velocity profile at the center-line showed that the material is being squeezed in the mushy zone since it is experiencing a reduction in thickness. Once the material reaches the coherency temperature, a high strain rate due to the squeezing is obtained and since the material is sensitive to strain rate at high temperature, a peak is observed in the stress at the center-line in the mushy zone. The high level of stress, consequently, causes a jump in the strain. Beyond the solidus temperature, the effective strain continues to increase gradually up to the maximum value and no more change is observed after the neutral point since the material is not deformed beyond this point. Fig. 17 shows ε_{eff} at the center-line affected by the casting speed for $\ell_1 = 32.5$ mm. As expected, less plastic deformation is experienced by the cast metal by increasing the casting speed since solidification front shifts toward the exit region.

The effective strain at the center-line for different set-back distances at $v = 2.0$ m/min is shown in Fig. 18. As the set-back distance increases for a final thickness of 6 mm, a slight increase in the effective strain is observed; however, for an entry thickness of 12 mm decreasing the final thickness leads to a dramatic increase of effective strain. Table 9 shows the reduction with respect to the thickness of the strip at which the strain starts to develop (t_{def}) at the center-line for each case and the corresponding effective strain at the exiting point of the caster ($\varepsilon_{\text{eff-max}}$). Obviously, more reduction experienced by

Table 8
Separating force (SF)–casting speed (v) relationship

Set-up no.	t_0 (mm)	t_f (mm)	ℓ_1 (mm)	SF–v Relationship
1	12	6	32.5	SF = 15.1372exp(−0.924v)
2	14	6	37.5	SF = 21.8184exp(−0.953v)
3	16	6	41.8	SF = 21.8252exp(−0.794v)
4	12	4	37.5	SF = 39.4656exp(−0.654v)
5	12	2	41.8	SF = 36.6052exp(−0.175v)

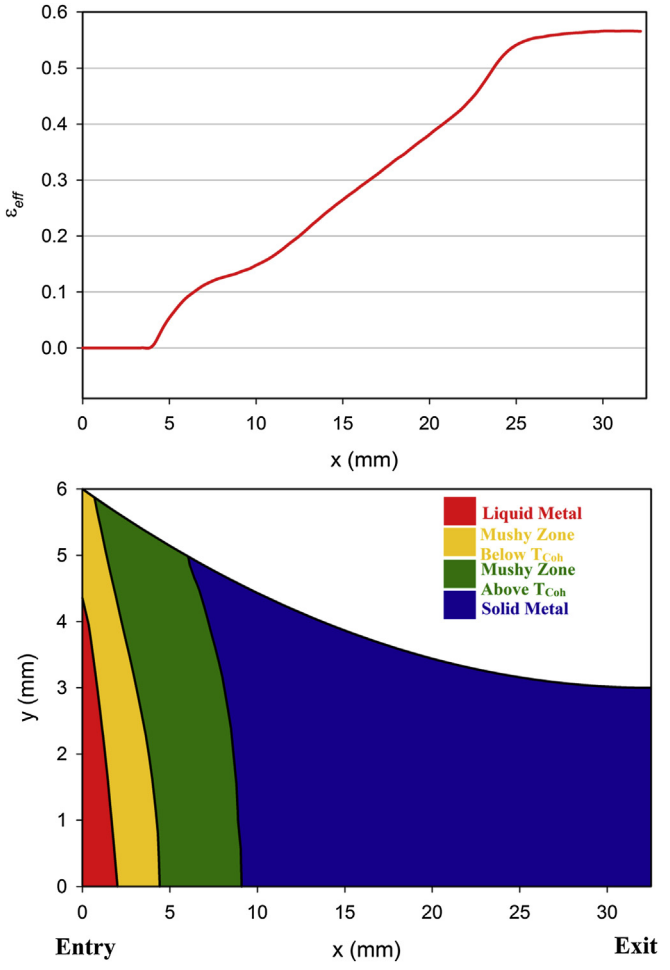

Fig. 16. Model-predicted effective strain (ε_{eff}) at the center-line (upper graph) in conjunction with the liquid–solid profile (lower graph) for $\ell_1 = 32.5$ mm and v=1.0m/min.

the solidified material causes higher effective strain at the exiting point of the caster.

Since roll-separating force is a typical parameter measured during TRC process, this parameter can be correlated to the

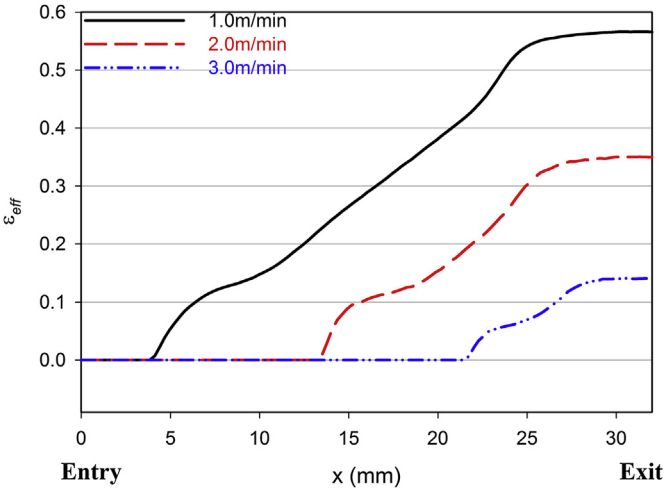

Fig. 17. Model-predicted effect of casting speed (v) on the effective strain at the center-line (ε_{eff}) for $\ell_1 = 32.5$ mm.

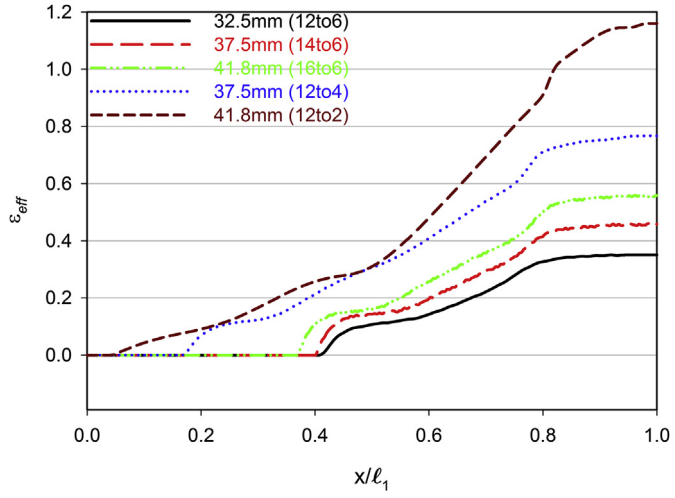

Fig. 18. Effect of set-back distance on the ε_{eff} development at the center-line for $v = 2.0$ m/min.

Table 9
The % reduction experienced by the solidified material for each set-up at $v = 2.0$ m/min.

Set-up no.	t_0 (mm)	t_f (mm)	ℓ_1 (mm)	t_{def} (mm)	Reduction (%)	$\varepsilon_{eff\text{-}max}$
1	12	6	32.5	7.97	32.83	0.35
2	14	6	37.5	8.80	46.7	0.46
3	16	6	41.8	9.89	64.83	0.56
4	12	4	37.5	9.39	134.75	0.77
5	12	2	41.8	5.29	164.5	1.16

amount of plastic deformation experienced by the cast strip during the process. A relationship between roll separating force and maximum effective strain at the center-line ($\varepsilon_{eff\text{-}max}$) was determined. Fig. 19 illustrates the $\varepsilon_{eff\text{-}max}$ versus SF per unit width of the strip for set-back distances with entry thickness of 12 mm. The correlation between two parameters for each set-up follows a logarithmic trend as shown by Eq. (23). The corresponding constants are presented in Table 10.

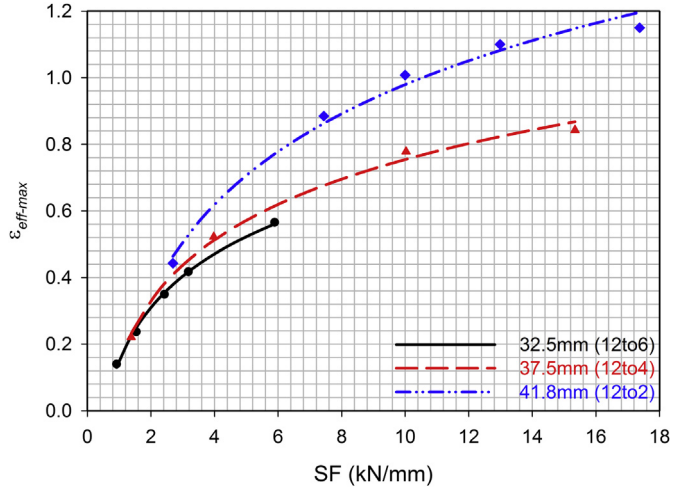

Fig. 19. Model-predicted relationship between maximum effective strain at the center-line ($\varepsilon_{eff\text{-}max}$) and roll separating force (SF) per unit width of the strip for different set-back distances and entry thickness of 12 mm.

Table 10
$\varepsilon_{eff\text{-}max}$–SF relationship.

Set-up No.	t_0 (mm)	t_f (mm)	ℓ_1 (mm)	$\varepsilon_{eff\text{-}max}$–SF relationship
1	12	6	32.5	$\varepsilon_{eff\text{-}max} = 0.3932\ln(SF) + 0.0743$
2	14	6	37.5	$\varepsilon_{eff\text{-}max} = 0.2638\ln(SF) + 0.1471$
3	16	6	41.8	$\varepsilon_{eff\text{-}max} = 0.2322\ln(SF) + 0.1485$
4	12	4	37.5	$\varepsilon_{eff\text{-}max} = 0.2024\ln(SF) + 0.2165$
5	12	2	41.8	$\varepsilon_{eff\text{-}max} = 0.2556\ln(SF) + 0.1634$

$$\varepsilon_{eff-max} = \gamma \ln(SF) + \delta \quad (23)$$

where $\varepsilon_{eff-max}$ is the maximum effective strain at the center-line and γ and δ are constants.

6. Conclusions

A two-dimensional thermal-fluid-stress mathematical model was developed and validated for the TRC of AZ31 magnesium alloy using the commercial FEM package, ALSIM. The current model was used to study the effect of set-back distance and casting speed. The validation was conducted by comparing the predicted and measured strip temperature at the exit point of the caster and the SDAS through the strip thickness. The important conclusions of this work include:

1. The microstructure of the as-twin roll cast AZ31 consists a chill zone at the strip surface, a columnar dendritic zone beneath the chill zone and an equiaxed dendritic zone at the center of strip. The finest SDAS was observed at the strip surface where the highest cooling rate is occurred and the largest SDAS was recognized at the strip center where lowest cooling rate is happened.
2. Increasing the casting speed and casting with shorter set-back distances causes higher temperature at the exit point of the caster. The relation between the casting speed and exit temperature seems to be linear and the exit temperature is more sensitive to set-back distance at higher casting speeds.
3. Lower level of normal stress on the strip surface is achieved when casting at higher speeds. Moreover, increasing the set-back distance leads to higher stress peak and a shift of stress development starting point toward the roll bite entry zone.
4. The roll separating force has a similar trend to strip surface normal stress; higher values are achieved at lower casting speeds and longer set-back distances. The relation between roll separating force and casting speed follows an exponential trend.
5. The cast strip experience higher effective strain at the center-line when it is cast with lower casting speed and longer set-back distance. The relationship between the maximum effective strain at the center-line and roll separating force was observed to be logarithmic.

6. Changing the set-back distance by varying the final thickness has more significant effect on the thermo-mechanical results than altering the nozzle entry thickness.

Acknowledgements

The authors of this work would like to appreciate the NSERC (Natural Sciences and Engineering Research Council of Canada) Magnesium Strategic Research Network (MagNET) for the financial support of this work and the Natural Resources Canada Government Materials Laboratory, CanmetMATERIALS located in Hamilton, Ontario for providing the opportunity to perform the experimental parts of the work. The assistance of Dr. M. Kozdras, Dr. A. Javaid, Dr. E. Essadiqi and Mr. G. Birsan and P. Newcombe (from CanmetMATERIALS) in processing the experimental data is gratefully acknowledged.

References

[1] H. Zhao, P. Li, L. He, Journal of Materials Processing Technology 211 (2011) 1197−1202.
[2] H.S. Di, Y.L. Li, Z.L. Ning, Z. Li, X. Liu, G.D. Wang, Materials Science Forum 488-489 (2005) 615−618.
[3] Y. Nakaura, A. Watanabe, K. Ohori, Materials Transactions 47 (2006) 1743−1749.
[4] J.W. Bae, C.G. Kang, S.B. Kang, Journal of Materials Processing Technology 191 (2007) 251−255.
[5] J. Zeng, R. Koitzsch, H. Pfeifer, B. Friedrich, Journal of Materials Processing Technology 209 (2009) 2321−2328.
[6] R.N. Grugel, Journal of Material Science 28 (1993) 677−683.
[7] M.S. Turhal, T. Savaskan, Journal of Material Science 38 (2003) 2639−2646.
[8] R.V. Allen, D.R. East, T.J. Johnson, W.E. Borbidge, D. Liang, Magnesium Alloy Sheet Produced by Twin Roll Casting, in: J.N. Hryn (Ed.), Magnesium Technology, TMS, Indianapolis, IN, USA, 2001, pp. 75−80.
[9] A. Baserinia, H. Ng, D.C. Weckman, M.A. Wells, S. Barker, M. Gallerneault, Metallurgical and Materials Transactions B 43B (2012) 887−901.
[10] H.G. Fjær, A. Mo, Metallurgical Transactions B 21B (1990) 1049−1061.
[11] D. Mortensen, M. Rudshaug, H.G. Fjær, Coupled Stress, Thermal and Fluid Flow Modelling in Materials Processing, in: H.I. Andersson, B. Skallerud (Eds.), Proceedings of MekIT'05 Third National Conference on Computational Mechanics, NTNU Tapir Academic Press, Trondheim, Norway, 2013, pp. 227−246.
[12] B.J. Howes, M.A. Wells, R. Bathla, D.M. Maijer, Constitutive Behaviour of As-Cast Magnesium Alloy AZ31 under Deformation Conditions Relevant to DC Casting, in: H. Kaufmann (Ed.), Proceedings of the Second International Light Metals Technology Conference, Wolfgang, Austria, 2005.
[13] D. Mortensen, ALSIM Reference Manual Version 6.1, Norway, 2011.
[14] ALSIM, Version: v5_r11, Institute for Energy Technology, Norway.
[15] H. Hao, D.M. Maijer, M.A. Wells, S.L. Cockcroft, D. Sediako, S. Hibbins, Metallurgical and Materials Transactions A 35A (2004) 3843−3854.
[16] X.D. Hu, D.Y. Ju, H.Y. Zhao, Materials Science Forum 539-543 (2007) 5037−5043.
[17] Y. He, A. Javaid, E. Essadiqi, M. Shehata, Canadian Metallurgical Quarterly 48 (2009) 145−156.
[18] H. Hao, D.M. Maijer, M.A. Wells, A. Phillion, S.L. Cockcroft, Metallurgical and Materials Transactions A 41A (2010) 2067−2077.